Possible depth-resolved reconstruction of shear moduli in the cornea following collagen crosslinking (CXL) with optical coherence tomography and elastography: supplement

GABRIEL REGNAULT,[1,*] MITCHELL A. KIRBY,[1] RUIKANG K. WANG,[1,2] TUENG T. SHEN,[2,3] MATTHEW O'DONNELL,[1] AND IVAN PELIVANOV[1]

[1]*Department of Bioengineering, University of Washington, Seattle, WA, USA*
[2]*Department of Ophthalmology, University of Washington, Seattle, WA, USA*
[3]*School of Medicine, University of Washington, Seattle, WA, USA*
*gregnaul@uw.edu

Supplement 1:

Possible depth-resolved reconstruction of shear moduli in the cornea following collagen crosslinking (CXL) with optical coherence tomography and elastography.

GABRIEL REGNAULT,[1*] MITCHELL A. KIRBY,[1] RUIKANG K. WANG[1,2], TUENG T. SHEN,[2,3] MATTHEW O'DONNELL[1] AND IVAN PELIVANOV[1]

[1]*Department of Bioengineering, University of Washington, Seattle, USA.*
[2]*Department of Ophthalmology, University of Washington, Seattle, USA.*
[3]*School of Medicine, University of Washington, Seattle, USA.*
*gregnaul@uw.edu

Section 1:

Guided mechanical wave propagation in a multi-layered NITI material

Assume that a CXL-treated cornea can be modelled as a laminate of NITI layers. Each layer has a finite thickness with defined in- and out-of-plane elastic moduli. The first layer is bounded on the top by air and the last layer is bounded on the bottom by a liquid to mimic corneal *in vivo* conditions. Because collagen fibers are oriented randomly in the equatorial plane, it possesses symmetry across fibers, *i.e.* in the direction normal to the corneal surface, which is mathematically described as transverse isotropy.

1.1. Dimensionless equations of motion in a multi-layered NITI material

Because the macroscopic corneal symmetry did not change following crosslinking, we assume that it contains at least two layers of finite thickness with distinct in- and out-of-plane shear moduli μ and G respectively. The density of every layer, ρ, is assumed to be identical for all layers and equal to that of the liquid bounding the lower layer, $\rho_l = \rho = 1000 \text{ kg·m}^{-3}$. Using Voigt's notation, the stress-strain relationship in each layer can be written as:

$$
\begin{bmatrix} \sigma_{xx} \\ \sigma_{yy} \\ \sigma_{zz} \\ \tau_{yz} \\ \tau_{xz} \\ \tau_{xy} \end{bmatrix} = \begin{bmatrix} \lambda + 2\mu & \lambda & \lambda & & & \\ \lambda & \lambda + 2\mu & \lambda & & & \\ \lambda & \lambda & \lambda + 2\mu + \delta & & & \\ & & & G & & \\ & & & & G & \\ & & & & & \mu \end{bmatrix} \begin{bmatrix} \epsilon_{xx} \\ \epsilon_{yy} \\ \epsilon_{zz} \\ \gamma_{yz} \\ \gamma_{xz} \\ \gamma_{xy} \end{bmatrix}, \tag{S1}
$$

where $\lambda = \rho c_p^2 - 2\mu$ is the Lamé coefficient, and c_p is the speed of the longitudinal wave that ensures incompressibility of the material (the Poisson's ratio of each layer taken individually is $\nu \sim 0.5$).

Newton's second law yields the wave equation of motion in terms of the displacement vector $\vec{u} = (u, v, w)$,

$$
\frac{\partial \sigma_{ij}}{\partial x_j} = \rho \frac{\partial u_i}{\partial t^2}. \tag{S2}
$$

Because our OCE experiments use AμT acting as a pseudo-line source, we can assume a plane-strain state (no displacement polarized along the y-axis: $v = 0$, and no propagation along the y-axis: $u = u(x,z), w = w(x,z)$). As such, in the NITI model, the equations of motion can be expressed as:

$$\rho u_{tt} = (\lambda + 2\mu)u_{xx} + Gu_{zz} + (\lambda + G)w_{xz}, \qquad \text{(S3)}$$
$$\rho w_{tt} = Gw_{xx} + (\lambda + 2\mu)w_{zz} + (\lambda + G)u_{xz}, \qquad \text{(S4)}$$

where the lower indexes indicate derivatives with time (t) or spatial coordinates (x, z).

By introducing the scales:

Position: $\quad x \sim h = \sum_i h_i$,
Displacement: $\quad u \sim h$,

Time: $\quad t \sim h \cdot \sqrt{\dfrac{\mu_M}{\rho}}$,

Frequency: $\quad f \sim \sqrt{\dfrac{\mu_M}{\rho}} \cdot \dfrac{1}{h}$,

Wavenumber: $\quad k \sim \dfrac{1}{h}$,

where h relates to the overall thickness, h_i to the thickness of the i_{th} layer, and $\mu_M = \max(\mu_i)$ is the maximum in-plane shear modulus among the layers. We can then define the dimensionless parameters $t^* = \dfrac{t}{h}\sqrt{\dfrac{\mu_M}{\rho}}, u^* = \dfrac{u}{h}, x^* = \dfrac{x}{h}, f^* = fh\sqrt{\dfrac{\rho}{\mu_M}}, k^* = kh$.

By applying this change of variables, we have:

$$\frac{\partial u}{\partial x} = \frac{\partial h \times u^*}{\partial x^*} \times \frac{\partial x^*}{\partial x} = h \cdot \frac{\partial u^*}{\partial x^*} \cdot \frac{1}{h} = \frac{\partial u^*}{\partial x^*}, \qquad \text{(S5)}$$

$$\frac{\partial^2 u}{\partial x^2} = \frac{\partial}{\partial x}\left(\frac{\partial u^*}{\partial x^*}\right) = \frac{1}{h} \cdot \frac{\partial^2 u^*}{\partial x^{*2}}, \qquad \text{(S6)}$$

$$\frac{\partial^2 u}{\partial t^2} = \frac{\mu_M}{\rho h} \cdot \frac{\partial^2 u^*}{\partial t^{*2}}, \qquad \text{(S7)}$$

which eventually leads to the dimensionless equations of motion:

$$\rho . u_{tt}^* \cdot \frac{\mu_M}{\rho h} = (\lambda + 2\mu)u_{xx}^* \cdot \frac{1}{h} + Gu_{zz}^* \cdot \frac{1}{h} + (\lambda + G)w_{xz}^* \cdot \frac{1}{h}, \qquad \text{(S8)}$$

$$\rho \mu_M \cdot w_{tt}^* \frac{\mu_M}{\rho h} = Gw_{xx}^* \cdot \frac{1}{h} + (\lambda + 2\mu)w_{zz}^* \cdot \frac{1}{h} + (\lambda + G)u_{xz}^* \cdot \frac{1}{h}, \qquad \text{(S9)}$$

and after rearranging:

$$u_{tt}^* = \beta^2 u_{xx}^* + \alpha^2 u_{zz}^* + \gamma^2 w_{xz}^*, \qquad \text{(S10)}$$
$$w_{tt}^* = \alpha^2 w_{xx}^* + \beta^2 w_{zz}^* + \gamma^2 u_{xz}^*, \qquad \text{(S11)}$$

with

$$\alpha^2 = \frac{G}{\mu_M}, \qquad \text{(S12)}$$

$$\beta^2 = \frac{(\lambda + 2\mu)}{\mu_M}, \qquad \text{(S13)}$$

$$\gamma^2 = \frac{(\lambda + G)}{\mu_M}. \qquad \text{(S14)}$$

For the sake of simplicity, we will later omit the asterisk '$*$' symbol to refer to dimensionless variables.

1.2. Dispersion relationship for guided mechanical waves in a multi-layered NITI material

Consider here a material containing multiple layers with identical density, each of finite thickness h_i. As such, there is a system of $[2 \times N]$ equations for the N layers:

$$u_{i,tt} = \beta_i^2 u_{xx} + \alpha_i^2 u_{zz} + \gamma_i^2 w_{xz} , \tag{S15}$$

$$w_{i,tt} = \alpha_i^2 w_{xx} + \beta_i^2 w_{zz} + \gamma_i^2 u_{xz} , \tag{S16}$$

$$\alpha_i^2 = \frac{G_i}{\mu_N} , \tag{S17}$$

$$\beta_i^2 = \frac{(\lambda_i + 2\mu_i)}{\mu_N} , \tag{S18}$$

$$\gamma_i^2 = \frac{(\lambda_i + G_i)}{\mu_N} . \tag{S19}$$

Assume harmonic solutions of the form:

$$u_i(x,z,t) = A_i e^{i(kx + l_i z - \omega t)} , \tag{S20}$$

$$w_i(x,z,t) = B_i e^{i(kx + l_i z - \omega t)} . \tag{S21}$$

Without loss of generality, assume $B_i = 1$. By substituting equations (S20) and (S21) into the equations of motion (S15) and (S16), the constants l_i and A_i can be determined for each frequency and wavenumber such that:

$$l_i = \pm \sqrt{\frac{1}{2}\left[\phi_i \pm \sqrt{\phi_i - 4q_{\alpha_i}^2 q_{\beta_i}^2}\right]} , \tag{S22}$$

$$A_i = \pm \left[-\frac{\sqrt{2}\frac{\gamma_i^2 k}{\alpha_i^2}\sqrt{\phi_i \pm \sqrt{\phi_i - 4q_{\alpha_i}^2 q_{\beta_i}^2}}}{\phi_i + \frac{2\beta_i^2}{\alpha_i^2}q_{\beta_i}^2 \pm \sqrt{\phi_i - 4q_{\alpha_i}^2 q_{\beta_i}^2}}\right] , \tag{S23}$$

where

$$\phi_i = \frac{\gamma_i^4 k^2}{\alpha_i^2 \beta_i^2} - \frac{\alpha_i^2}{\beta_i^2}q_{\alpha_i}^2 - \frac{\beta_i^2}{\alpha_i^2}q_{\beta_i}^2 , \tag{S24}$$

$$q_{\alpha_i}^2 = k^2 - \frac{\omega^2}{\alpha_i^2} , \tag{S25}$$

$$q_{\beta_i}^2 = k^2 - \frac{\omega^2}{\beta_i^2} . \tag{S26}$$

The full solutions for a given layer can be expressed as the combination of 4 partial waves:

$$u_i(x,z,t) = \sum_{j=1}^4 C_{i,j} A_{i,j} e^{i l_{i,j} z} e^{i(kx - \omega t)} , \tag{S27}$$

$$w_i(x,z,t) = \sum_{j=1}^4 C_{i,j} e^{i l_{i,j} z} e^{i(kx - \omega t)} . \tag{S28}$$

In the fluid, the dimensionless velocity potential is:

$$\Phi = C_{N,5} e^{\epsilon z} e^{i(kx - \omega t)} , \tag{S29}$$

where $\epsilon = \sqrt{k^2 - \frac{\omega^2}{\delta^2}}$ and $\delta^2 = \frac{\rho}{\mu_N}c_p^2$.

The constants $C_{i,j}$ are chosen so that the solutions satisfy the boundary conditions.

3

Traction free air-solid interface sets

$$\sigma_{1,xz} = 0 \qquad \text{at} \qquad z_1 = 1, \qquad \text{(S30)}$$
$$\sigma_{1,zz} = 0 \qquad \text{at} \qquad z_1 = 1. \qquad \text{(S31)}$$

Continuity of normal components of stress and displacement between each layer give

$$\sigma_{i,xz} = \sigma_{i+1,xz} \qquad \text{at} \qquad z_i = 1 - \frac{\sum_{k=1}^{i} h_k}{h}, \qquad \text{(S32)}$$

$$\sigma_{i,zz} = \sigma_{i+1,zz} \qquad \text{at} \qquad z_i = 1 - \frac{\sum_{k=1}^{i} h_k}{h}, \qquad \text{(S33)}$$

$$u_i = u_{i+1} \qquad \text{at} \qquad z_i = 1 - \frac{\sum_{k=1}^{i} h_k}{h}, \qquad \text{(S34)}$$

$$w_i = v_{i+1} \qquad \text{at} \qquad z_i = 1 - \frac{\sum_{k=1}^{i} h_k}{h}. \qquad \text{(S35)}$$

Medium-fluid boundary conditions (zero tangential stress, continuity of normal stress components and speed) set

$$\sigma_{N,xz} = 0 \qquad \text{at} \qquad z_N = 0, \qquad \text{(S36)}$$
$$\sigma_{N,zz} = \sigma_{zz}^{f} \qquad \text{at} \qquad z_N = 0, \qquad \text{(S37)}$$
$$\dot{w}_N = \dot{w}^{f} \qquad \text{at} \qquad z_N = 0. \qquad \text{(S38)}$$

Substituting the general solution into the boundary conditions yields a $[4N+1 \times 4N+1]$ homogeneous system for the coefficient: $\mathbf{Mc = 0}$. This system has a nontrivial solution if and only if the determinant of $\mathbf{M}$ (see Eq. (S39) below) is zero. For a given angular frequency ω, the wavenumber k associated with different wave types (pure shear or guided modes) can be found by minimizing the absolute value of the determinant:

$$M = \begin{vmatrix}
(l_{1,1}A_{1,1} + k)e^{il_{1,1}} & (l_{1,2}A_{1,2} + k)e^{il_{1,2}} & (l_{1,3}A_{1,3} + k)e^{il_{1,3}} & (l_{1,4}A_{1,4} + k)e^{il_{1,4}} & \\
[k(\gamma_1^2 - \alpha_1^2)A_{1,1} + \beta_1^2 l_{1,1}]e^{il_{1,1}} & k(\gamma_1^2 - \alpha_1^2)A_{1,2} + \beta_1^2 l_{1,2}]e^{il_{1,2}} & k(\gamma_1^2 - \alpha_1^2)A_{1,3} + \beta_1^2 l_{1,3}]e^{il_{1,3}} & k(\gamma_1^2 - \alpha_1^2)A_{1,4} + \beta_1^2 l_{1,4}]e^{il_{1,4}} & \\
(l_{1,1}A_{1,1} + k)e^{il_{1,1}z_2} & (l_{1,2}A_{1,2} + k)e^{il_{1,2}z_2} & (l_{1,3}A_{1,3} + k)e^{il_{1,3}z_2} & (l_{1,4}A_{1,4} + k)e^{il_{1,4}z_2} & \\
[k(\gamma_1^2 - \alpha_1^2)A_{1,1} + \beta_1^2 l_{1,1}]e^{il_{1,1}z_2} & k(\gamma_1^2 - \alpha_1^2)A_{1,2} + \beta_1^2 l_{1,2}]e^{il_{1,2}z_2} & k(\gamma_1^2 - \alpha_1^2)A_{1,3} + \beta_1^2 l_{1,3}]e^{il_{1,3}z_2} & k(\gamma_1^2 - \alpha_1^2)A_{1,4} + \beta_1^2 l_{1,4}]e^{il_{1,4}z_2} & \\
A_{1,1}e^{il_{1,1}z_2} & A_{1,2}e^{il_{1,2}z_2} & A_{1,3}e^{il_{1,3}z_2} & A_{1,4}e^{il_{1,4}z_2} & \\
e^{il_{1,1}z_2} & e^{il_{1,2}z_2} & e^{il_{1,3}z_2} & e^{il_{1,4}z_2} & \\
0 & 0 & 0 & 0 & \\
\vdots & \vdots & \vdots & \vdots & \\
0 & 0 & 0 & 0 & \cdots \\
0 & 0 & 0 & 0 & \cdots \\
-(l_{2,1}A_{2,1} + k)e^{il_{2,1}z_2} & -(l_{2,2}A_{2,2} + k)e^{il_{2,2}z_2} & -(l_{2,3}A_{2,3} + k)e^{il_{2,3}z_2} & -(l_{2,4}A_{2,4} + k)e^{il_{2,4}z_2} & \cdots \\
-[k(\gamma_2^2 - \alpha_2^2)A_{2,1} + \beta_2^2 l_{2,1}]e^{il_{2,1}z_2} & -[k(\gamma_2^2 - \alpha_2^2)A_{2,2} + \beta_2^2 l_{2,2}]e^{il_{2,2}z_2} & -[k(\gamma_2^2 - \alpha_2^2)A_{2,3} + \beta_2^2 l_{2,3}]e^{il_{2,3}z_2} & -[k(\gamma_2^2 - \alpha_2^2)A_{2,4} + \beta_2^2 l_{2,4}]e^{il_{2,4}z_2} & \cdots \\
-A_{2,1}e^{il_{2,1}z_2} & -A_{2,2}e^{il_{2,2}z_2} & -A_{2,3}e^{il_{2,3}z_2} & -A_{2,4}e^{il_{2,4}z_2} & \cdots \\
-e^{il_{2,1}z_2} & -e^{il_{2,2}z_2} & -e^{il_{2,3}z_2} & -e^{il_{2,4}z_2} & \cdots \\
0 & 0 & 0 & 0 & \cdots \\
\vdots & \vdots & \vdots & \vdots & \vdots \\
0 & 0 & 0 & 0 & 0 \\
\vdots & \vdots & \vdots & \vdots & \vdots \\
l_{N,1}A_{N,1} + k & l_{N,2}A_{N,2} + k & l_{N,3}A_{N,3} + k & l_{N,4}A_{N,4} + k & 0 \\
k(\gamma_N^2 - \alpha_N^2)A_{N,1} + \beta_N^2 l_{N,1} & k(\gamma_N^2 - \alpha_N^2)A_{N,2} + \beta_N^2 l_{N,2} & k(\gamma_N^2 - \alpha_N^2)A_{N,3} + \beta_N^2 l_{N,3} & k(\gamma_N^2 - \alpha_N^2)A_{N,4} + \beta_N^2 l_{N,4} & \frac{\omega \rho^f}{\rho} \\
\omega & \omega & \omega & \omega & -i\epsilon
\end{vmatrix}. \quad \text{(S39)}$$

Section 2:

Experimental validation of the analytical multi-layer model in bilayer isotropic phantoms

While FEM simulations in Onscale demonstrated the appropriateness of the multi-layer framework, here we provide additional experimental validation using isotropic phantoms.

Agarose phantoms were prepared using different agar concentrations. Four different phantoms were made. The first two phantoms (Phantom A and Phantom B, Table S1) represented homogeneous single layers with different stiffness, in which three (3) and two (2) wt. % of agar were used respectively. Titanium nanoparticles were added to the mixtures (respectively 0.1 and 0.2 wt % TiO_2) to create optical scattering and enable differentiation of phantom structures. Both phantoms were isotropic.

Two bilayer phantoms were made of the same concentration of agar and TiO_2. Phantom C had a stiffer layer on the top of the softer layer. The stiffer solution was brought to 90°C and poured into a petri dish for solidification. Its thickness was about 500 μm. Then the softer solution was brought to 90°C and poured on top off the stiff layer. Phantom D had the opposite layer orientation (see Table S1). The image-based calculated total thickness was 1000 μm ± 9 μm, with approximately 2/3 of the full thickness for the top layer and 1/3 for the bottom layer. Elastic moduli of the layers in the bilayer phantoms were assumed equal to those for single layers (Phantoms A and B). For all experiments, the phantoms were laying on top of a liquid bath, replicating corneal boundary conditions.

Table S1. Phantom properties.

	Agar (w.t %)	TiO_2 (w.t %)	Thickness, h (μm)	Stiffness, G (kPa)
Single layer phantoms				
Phantom A	2	0.4	996 ∓ 1	216 ± 2
Phantom B	3	0.2	777 ± 30	84 ± 5
2-layer phantoms				
Phantom C	-	-	1000 ± 9	-
Stiff (top)	3	0.2	690 ± 25	211 ± 7 (from 2-layer model fitting)
Soft (bottom)	2	0.4	310 ± 25	84 ± 5 (assumed equal to Phantom B)
Phantom D	-	-	942 ± 2	-
Soft (top)	2	0.4	242 ± 20	84 ± 5 (assumed equal to Phantom B)
Stiff (bottom)	3	0.2	700 ± 20	225 ± 5 (from 2-layer model fitting)

2.1. Elasticity of single layer phantoms

The spatio-temporal wavefields of the control phantoms and their associated frequency-wavenumber spectra are shown respectively in Figs. S1(a), (b) for Phantom A and Figs. S1(c), (d) for Phantom B. The fits are performed assuming an isotropic medium where only the A_0-mode is considered. We measured $G_{soft}^{control} = 84$ kPa ± 5 kPa and $G_{stiff}^{control} = 216$ kPa ± 2 kPa (see Table S1). The mean values and error bars are obtained from a statistical analysis over 5 scans repeated at the same location. These values serve as the baseline to analyze experiments in bilayer phantoms.
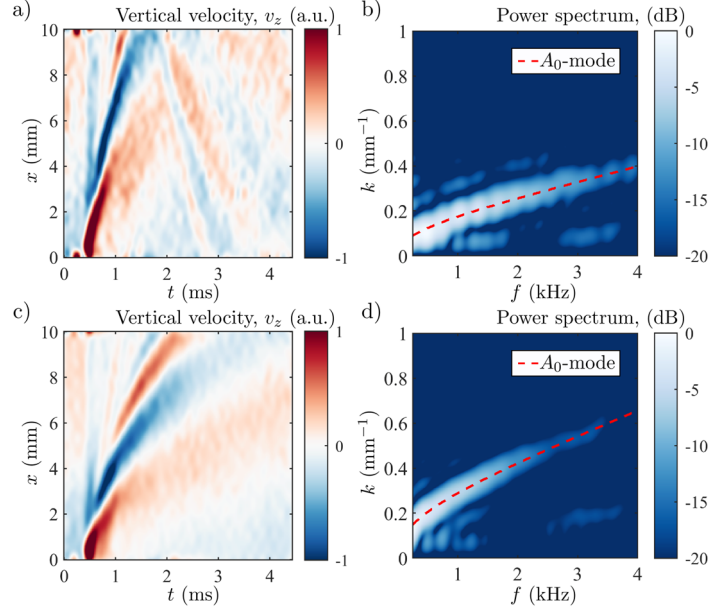

Fig. S1. Spatio-temporal wavefields (*x-t* plots) and their associated frequency-wavenumber (*f*-*k*) spectra; (a), (b) Phantom A (stiffer); (c), (d) Phantom B (softer). In (b) and (d), the best fit solution of the A_0-mode is indicated in red.

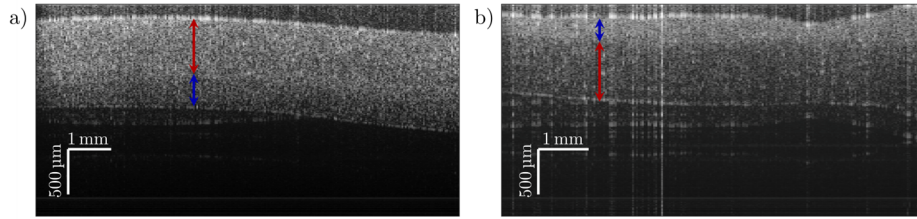## 2.2. Guided waves in bilayer phantoms

Fig. S2. Structural images of the bilayer agar phantom at two different locations with (a) Phantom C (harder part on the top, see Table S1) and (b) Phantom D (softer part on the top, see Table S1). Red and blue arrows, respectively, indicate the thickness of stiffer and softer layers.

Structural images of the bilayer phantom are shown in Fig. S2. The images correspond to two different locations of the same phantom, where: (a) the stiffer layer (on top) takes approximately 2/3 of the total thickness (Phantom C); (b) the bilayer phantom is reversed upside-down, and the stiffer layer (at the bottom) takes approximately 3/4 of the total thickness

(Phantom D). Note that the external interface of the stiffer layer is smoother because it was in contact with the mold during polymerization while the softer layer was in contact with air. The average thicknesses for Phantoms C and D were respectively $h = 1000\ \mu m \pm 9\ \mu m$ and $h = 942\ \mu m \pm 2\ \mu m$. The mean values and error bars are obtained from a statistical analysis over 5 scans repeated at the same location. The parameters of all phantoms are given in Table S1.
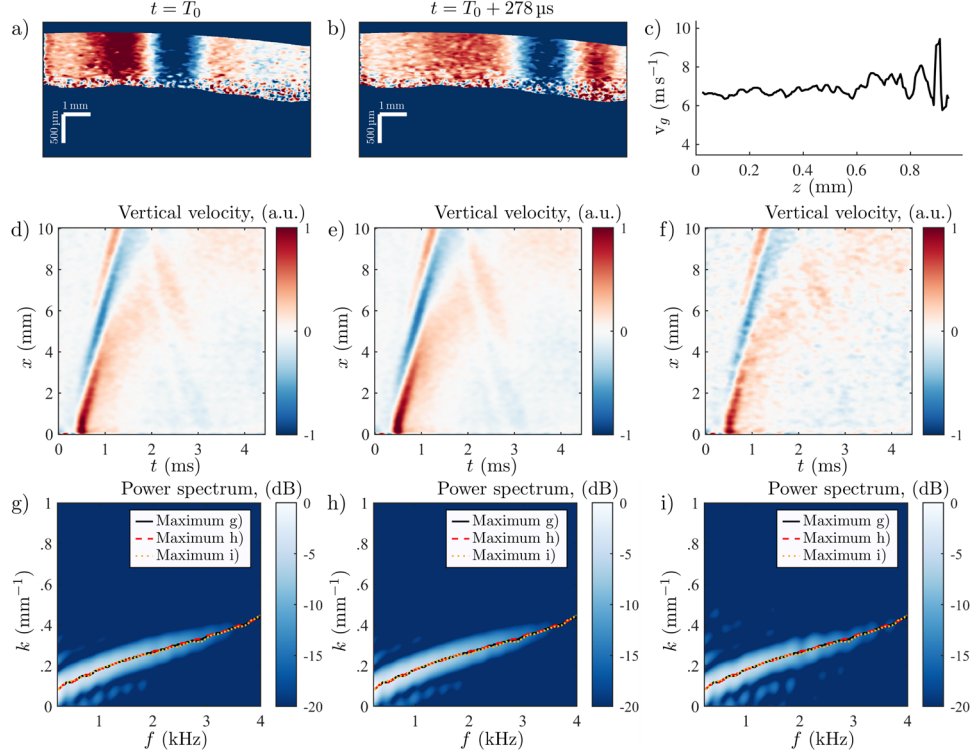

Fig. S3. In-depth analysis of the guided wavefield in Phantom C, shown in Fig. S1(a). (a), (b) Snapshots of the wavefields (x-t plots) at two time-instants separated by 278 μs. (c) In-depth profile of the group velocity measured using correlation. (d), (e), (f) Spatio-temporal wavefield averaged respectively over: (d) the total thickness; (e) the top layer; (f) the bottom layer. (g), (h), (i) f-k spectra associated respectively with the x-t plots shown in (d), (e), (f). The maximum wavenumber detected for each frequency of the spectrum and for each case are displayed on top of the spectra.

As observed in the control phantoms (Fig. S2), the A_0-mode dominates for such stiffness and thickness. Similar to CXL-treated corneas, we expect the A_0-mode to dominate as well in the bilayer phantom. Figure S3 illustrates this for Phantom C (stiffer layer on top). Figures S3(a), (b) show snapshots of the 2D-wavefields at two different time instants. The A_0-mode clearly dominates and occupies the whole thickness, with no noticeable variation between layers. First, we applied a geometric correction to the wavefield to account for the slight curvature of the phantoms. Then, we measured the group velocity of the wavefield over depth (see Fig. S3(c)) using correlation and confirmed that the mode has a constant speed over depth, with an average group velocity of about 7 m/s.

The SNR decreases in the posterior region of the phantoms due to artificial mirror images of the phantom within the field of view. This impacts the precision of group velocity measurements, as can be seen in Fig. S3(c). If guided wave behavior is ignored, which means that the group and phase velocities are identical, then the elasticity of the phantoms would be estimated using the well-known formula: $G = \rho v_g^2 \approx 50$ kPa. This value is almost two times less than the elasticity measured for the softer layer, and over four times less than that of the

harder layer. Clearly, a simple estimate based on the group velocity is erroneous and does not provide in-depth information; guided wave analysis is required.

To confirm our first observations with the group velocity, we also measured how x-t plots, and ultimately f-k spectra, varied with depth. These results are shown in Figs. S3(d-i) with: (d), (g) - the wavefield averaged over the whole depth and its associated f-k spectrum; (e), (h) - the wavefield averaged over depth in the top layer and its associated f-k spectrum; (f), (i) - the wavefield averaged over depth in the bottom layer and its associated f-k spectrum. For comparison, the maximum wavenumber of the spectrum for each frequency was measured and displayed on top of the three cases: they are nearly an exact match! This confirms that the guided wavefield, dominated by the A_0-mode, does not vary with depth. Guided wave propagation completely mixes phantom properties, and data acquired at different depths cannot be used for direct depth-resolved moduli reconstruction.
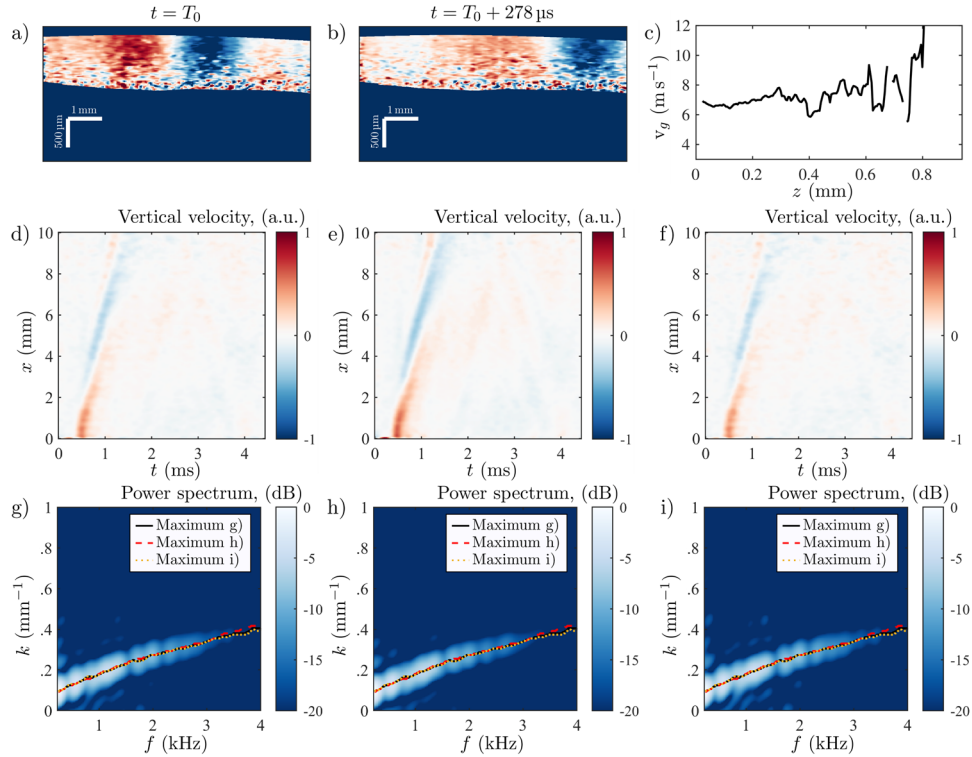

Fig. S4. In-depth analysis of the guided wavefield in Phantom D shown in Fig. S1(b). (a), (b) Snapshots of the wavefields (x-t plots) at two time-instants separated by 278 µs. (c) In-depth profile of the group velocity measured using correlation. (d), (e), (f) Spatio-temporal wavefield averaged respectively over: (d) the total thickness; (e) the top layer; (f) the bottom layer. (g), (h), (i) f-k spectra associated respectively with the x-t plots shown in (d), (e), (f). The maximum wavenumbers detected for each frequency of the spectrum and for each case are displayed on top of the spectra.

In contrast, our model can reconstruct individual layer properties via the dependence of the A_0-mode on individual layer parameters. Because guided A_0-modes are the same at all depths, they can be acquired at any surface or at any depth, or averaged over the depth even if the material stiffness varies with depth. This is also an advantage for the proposed reconstruction method.

Identical in-depth processing was applied to Phantom D, *i.e.*, when the phantom is reversed upside-down, and the stiff layer is at the bottom. The results are summarized in Fig. S4 and show similar features to those discussed above with Fig. S3.

2.3. Elasticity of the bilayer phantoms

Because the total thickness of the bilayer phantoms is known, and the respective thickness and baseline stiffness of each layer is also known, we can now fit the stiffer layer using the analytical model and the method introduced in this paper and compare to the known properties. To replicate the method used for the cornea sample, we fixed the value of the softer layer so that $G_{soft} = G_{soft}^{control} = 84$ kPa $\pm$ 4 kPa. We then searched for a maximum of goodness of fit while G_{stiff} was varied within a broad range of elasticity values. The goodness of fit is shown in Fig. S5(a) for Phantom C and in Fig. S5(b) for Phantom D. The best fit solutions are displayed on the f-k spectrum associated with each case in Figs. S5(c), (d). Using this method, we measured the stiffer layer to be on average $G_{stiff}^{2lay} = 211$ kPa $\pm$ 7 kPa and $G_{stiff}^{2lay} = 225$ kPa $\pm$ 5 kPa for, respectively, Phantoms C and D (see Table S1). The mean values and error bars are obtained from a statistical analysis over 5 scans repeated at the same location. These results are in good agreement with the expected value for the stiffer layer measured from the control phantom: $G_{stiff}^{control} = 215$ kPa $\pm$ 2 kPa.
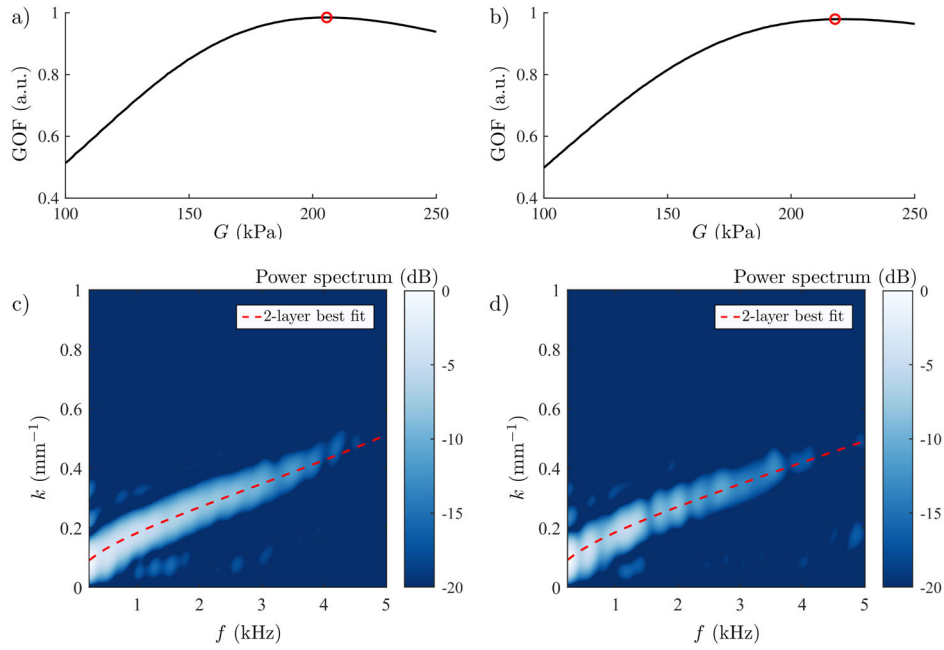

Fig. S5. Fitting f-k spectrum of the bilayer phantoms. The softer layer elasticity is fixed and the best fit is sought by varying the elasticity of the stiffer part and evaluating the goodness of fit (GOF) between the measured spectrum and the analytical A_0-mode dispersion curve obtained with the 2-layer model. (a) GOF curve for the case shown in Fig. S1(a), *i.e.,* the stiffer part on top. (b) GOF curve for the case shown in Fig. S1(b), *i.e.,* the softer part on on top. The red circle indicates the optimum. (c), (d) f-k spectra associated with the cases shown above. The red dashed curve shows the A_0-mode dispersion curve corresponding to the best fit solution.

Overall, the experiments on isotropic phantoms confirm the soundness of the theoretical framework and processing technique to assess in-depth elasticity variation with guided mechanical waves in soft tissues such as the cornea. Although the phantoms considered here are isotropic, we believe that these phantom studies well justify the approach introduced for anisotropic cornea layers. Numerical simulations also fully confirm depth-independent guided wavefields, spectra, and group velocities in media with depth-varying elastic properties.

Section 3:

Effective A_0-mode for a multi-layered NITI medium

3.1. Do engineering moduli correctly define the effective guided mechanical wave in a multi-layered NITI medium?

As discussed in Section 3.3 of the main manuscript, elastic moduli determined for all layers of CXL-treated cornea can be used to compute effective corneal engineering moduli, where μ_{eff} uses a simple mixture rule (Eq. (5) of the main manuscript) whereas G_{eff} requires the inverse mixture rule (Eq. (4) of the main manuscript).

We also checked whether this model can describe guided wave behavior in the partially crosslinked cornea when considered as an effective homogeneous material. First, we applied the fitting procedure to the treated cornea, considering it as a single layer with 'effective' moduli (see Fig. S6). We could determine a pair of moduli for the computed f-k spectrum that best fit the A_0-mode. These effective 'guided wave' elastic moduli were $G_{guided} = 127.5$ kPa $\mp (12, 17)$ kPa and $\mu_{guided} = 9.3$ MPa $\mp (8, 18)$ MPa, with a $\Phi = 0.953$ goodness of fit.

These values clearly do not equal the corneal effective engineering moduli, $G_{eff} = 77.3$ kPa $\mp (6, 10)$ kPa and $\mu_{eff} = 15.4$ MPa $\mp (8, 11)$MPa, computed with the mixture rules described by Eqs. (4), (5) using moduli measured with OCE in both layers. That is, it appears that the effective guided wave behavior in a multi-layered NITI medium is not described by the corneal effective engineering moduli determining its low-frequency quasi-static deformation.
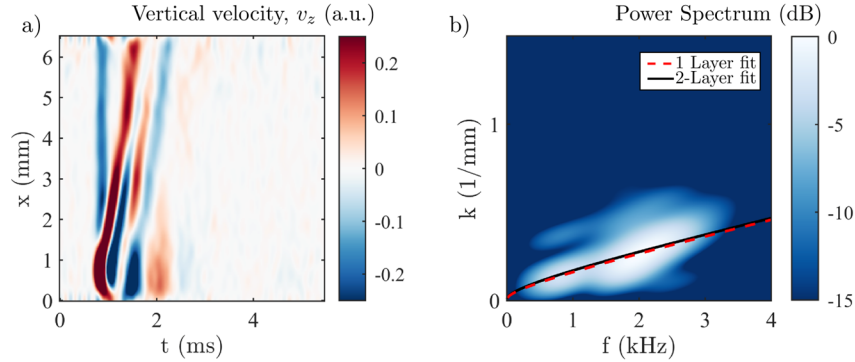

Fig. S6. Fitting experimental results obtained for a partially (in-depth) CXL-treated cornea with either 1- or 2-layer analytical model. (a) Measured vertically polarized top-surface vibration velocity field (*x-t* plot) of the guided wave. (b) Its 2D-FFT spectrum with best-fit dispersion curves for 1-layer (red dashed line) and 2-layer (black solid line) models superimposed.

3.2. A single-layer approximation for the computation the guided mechanical wave dispersion in a multi-layered NITI medium

Using our analytical model, we further investigated the accuracy of the mixture rule (Eqs. (4) and (5)) to predict the effective 'guided wave' behavior. We considered different distributions of stiffness: i) a two-layer case, as assumed for CXL-treated corneas; ii) a five-layer case with random distribution of stiffness and thickness of the layers; iii) a medium with both G and μ following an exponential decay in stiffness from top to bottom. In all cases, the total medium thickness was $h = 500$ µm and its top and bottom layers replicated the corneal boundary conditions. Matlab scripts to reproduce these results are provided in Ref. [1].

Results for case i) are presented in Fig. S7 for a material containing two layers with $G_{ant} = 300$ kPa and $\mu_{ant} = 30$ MPa, and $G_{pos} = 60$ kPa and $\mu_{pos} = 5$ MPa. For this case,

we also explore different ratios between thicknesses of anterior and posterior layers. Results show that the A_0-mode computed with the effective engineering moduli using the mixture rules of Eqs. (4) and (5) does not match the exact analytical solution computed using the individual stiffness moduli of the layers, *i.e.*, using the 2-layered model directly. The difference is especially pronounced in the high-frequency range.

Results for case ii) are presented in Fig. S8. The distribution of stiffness for respectively G and μ are shown in Figs. S8(b), (c). The thicknesses of layers were random with the total thickness of $h = 500$ μm. As for case i), we also see that assuming a single layer material with averaged moduli computed using engineering effective mechanical moduli does not accurately predict A_0-mode dispersion.
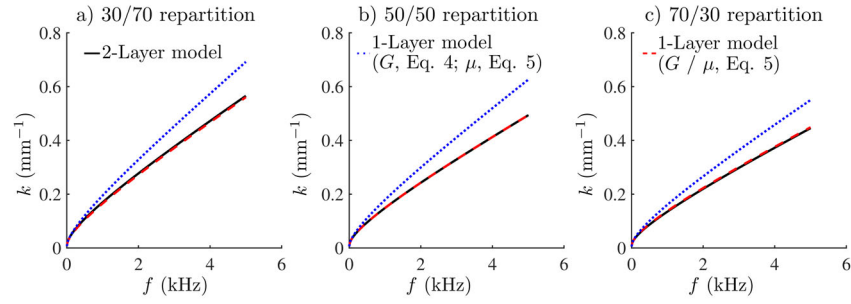

Fig. S7. A₀-mode dispersion spectrum computed using different models and sets of mechanical moduli. In all 3 panels, black solid line corresponds to the exact solution obtained with the 2-layer model; blue dotted line corresponds to a 1-layer model with effective engineering mechanical moduli (Eq. (4) for G and Eq. (5) for μ); red dashed line corresponds to a 1-layer model with both effective moduli computed with Eq. (5). Three different thicknesses of the top layer are considered (a) 150 μm (30/70 repartition), (b) 250 μm (50/50 repartition), and (c) 350 μm (70/30 repartition). Elastic moduli of the top layer are $G_{ant} = 300$ kPa and $\mu_{ant} = 30$ MPa and for the bottom layer are $G_{pos} = 60$ kPa and $\mu_{pos} = 5$ MPa, and the total thickness is $h = 500$ μm for all 3 cases.
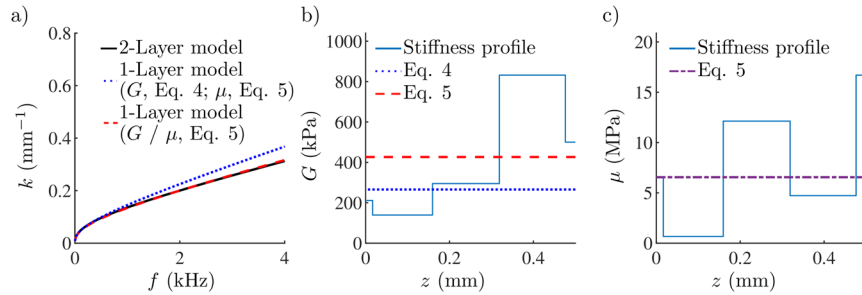

Fig. S8. A₀-mode dispersion spectrum computed in a 5-layer medium using different models and sets of mechanical moduli. In panel (a), black solid line corresponds to the exact solution obtained with the 2-layer model; blue dotted line corresponds to a 1-layer model with effective engineering mechanical moduli (Eq. (4) for G and Eq. (5) for μ); red dashed line corresponds to a 1-layer model with both effective moduli computed with Eq. (5). (b) Distribution of modulus G in the 5-layer medium (light blue solid line), and its effective value obtained with Eq. (4) (blue dotted line) and with Eq. (5) (red dashed line). (c) Distribution of modulus μ in the 5-layer medium (light blue solid line), and its effective value obtained with Eq. (5) (purple dash-dotted line). Total thickness of the medium is $h = 500$ μm.

Results for case iii) are presented in Fig. S9. The distribution of stiffness for respectively G and μ are shown in Figs. S9(b), (c). We considered 10 layers where G decreased exponentially from 500 kPa on top to 50 kPa at the bottom and μ decreased exponentially as well from 20 MPa on top to 2 MPa at the bottom. As for both cases i) and ii), the effective mechanical moduli do not describe the dispersion curve accurately, especially over the high-frequency range.
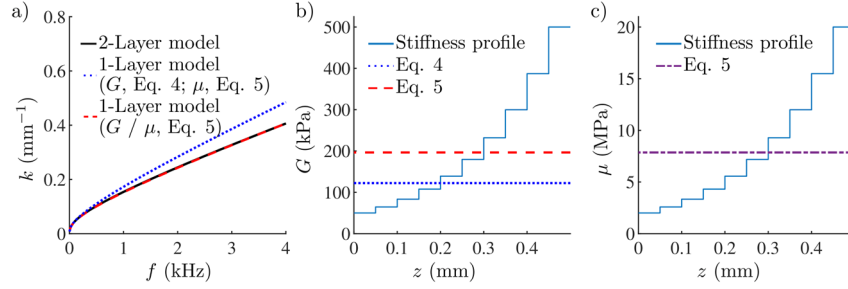

Fig. S9. A_0-mode dispersion spectrum computed in a 10-layer medium with an exponential decay of elastic moduli using different models and sets of mechanical moduli. In panel (a), black solid line corresponds to the exact solution obtained with the 2-layer model; blue dotted line corresponds to a 1-layer model with effective engineering mechanical moduli (Eq. (4) for G and Eq. (5) for μ); red dashed line corresponds to a 1-layer model with both effective moduli computed with Eq. (5). (b) Distribution of modulus G in the 5-layer medium (light blue solid line), and its effective value obtained with Eq. (4) (blue dotted line) and with Eq. (5) (purple dash-dotted line). (c) Distribution of modulus μ in the 5-layer medium (light blue solid line), and its effective value obtained with Eq. (5) (red dashed line). Total thickness of the medium is $h = 500$ μm.

Thus, we can conclude that the mixture rules providing effective engineering moduli of multi-layered NITI media do not accurately describe guided wave behavior. As such, reconstruction of effective moduli from OCE measurements in a partially CXL-treated cornea should be performed with care.

The second question is which mixture model would describe guided wave behavior in a partially CXL-treated cornea with reasonable accuracy. This is an open and non-trivial question outside the scope of this paper. However, as shown in Figs. S7, S8 and S9, a simple direct mixture rule for both in- and out-of-plane moduli (Eq. (5)) produces a dispersion curve closely matching the N-layer model.

For the two-layer case (Fig. S7), equal thickness layers (50/50 split ratio, Fig. S7(b)) show a near-exact match, while the larger the difference between the layer thicknesses, the larger the difference between the solutions, although this difference remains small. In Fig. S8 (random thickness distribution), the simple mixing rule provides a reasonably good match, even though there is a small difference in the dispersion curves. In Fig. S9 (exponential decay of moduli), there is an almost exact match between the single layer effective model and the N-layer case.

Based on this observation, we assume that a simple mixture rule applied to both mechanical moduli μ and G provides a reasonable description of guided wave dispersion in multi-layer NITI materials. Note that this remark also extends to isotropic nearly incompressible composites. The effective guided model and the exact N-layer solution only differ slightly for an unequal distribution of thicknesses. However, we note that this rule is empirical and is not theoretically proven. Finding an exact analytical solution may be difficult and include frequency-dependent terms. This is a subject for future studies.

References:

[1] G. Regnault, Mitchell A. Kirby, Ruikang K. Wang, Tueng T. Shen, Matthew O'Donnell and Ivan Pelivanov." Matlab tools for guided waves in composite nearly incompressible materials," figshare (2023), https://doi.org/10.6084/m9.figshare.23504652.